Magnetism of Fe, Co and Ni nanowires in self-assembled arrays

2001 J. Phys.: Condens. Matter 13 R433

(http://iopscience.iop.org/0953-8984/13/25/201)

INSTITUTE OF PHYSICS PUBLISHING JOURNAL OF PHYSICS: CONDENSED MATTER

J. Phys.: Condens. Matter **13** (2001) R433–R460 www.iop.org/Journals/cm PII: S0953-8984(01)20158-1

TOPICAL REVIEW

Magnetism of Fe, Co and Ni nanowires in self-assembled arrays

D J Sellmyer, M Zheng and R Skomski

Department of Physics and Astronomy and Center for Materials Research and Analysis, University of Nebraska, Lincoln, NE 68588, USA

Received 15 December 2000, in final form 6 April 2001

Abstract

Recent work on magnetic properties of transition-metal nanowire arrays produced by electro-deposition is reviewed. The wires, which are electro-deposited into self-assembled porous anodic alumina, form nearly hexagonal arrays characterized by wire diameters down to less than 10 nm, wire lengths up to about 1 μm, and variable centre-to-centre spacings of the order of 50 nm. The fabrication and structural characterization of the arrays is summarized, magnetic data are presented and theoretical explanations of the behaviour of the wires are given. Emphasis is on extrinsic phenomena such as coercivity, magnetization reversal and interactions of the magnetic nanowires. In particular, we analyse how wire imperfections give rise to magnetic localization and dominate the hysteresis behaviour of the wires. Potential applications are outlined in the last section.

1. Introduction

Periodic arrays of magnetic nanowires deposited in self-assembled alumina templates have recently attracted much attention. The arrays have many potential applications in technology, for example in high-density magnetic recording and as sensors, and are scientifically interesting because they can be considered as model systems to study interaction processes and magnetic reversal in low-dimensional magnetic structures.

A traditional method to produce periodic arrays of nanoscale magnetic particles, dots, and wires is nanolithography [1, 2]. However, that method is comparatively cumbersome and not suitable for large-area production. Here we investigate an alternative approach which exploits a naturally occurring process, namely the self-assembly of porous media, as a vehicle for fabrication [3–5]. This approach is promising for large-area nanopatterning with high aspect ratio, which is usually difficult to achieve by conventional lithography. Molecular sieves [6], track-etched polymer membranes [7, 8] and porous anodic alumites [5] are some representative templates. In the case of nanowires, porous anodic alumites are considered as particularly attractive template materials for fabricating nanowires, because the pore density is high, the pore distribution is uniform and the diameter of the pores is small [9].

0953-8984/01/250433+28$30.00

Porous alumina, created by anodization of aluminium in acidic electrolytes, contains cylindrical and uniformly sized pores whose diameter ranges from 4 to 200 nm, depending on the anodization conditions. The pores, whose length ranges from less than 20 nm to about 1 μm, form an ordered array of columnar hexagonal cells [10]. Figure 1 shows scanning electron microscopy (SEM) images of a typical sample. Metals and semiconductors have been electrochemically deposited into these pores, and the resulting materials may be used, for example, as magnetic recording media [11, 12], optical devices [13] and electroluminescent display devices [14].

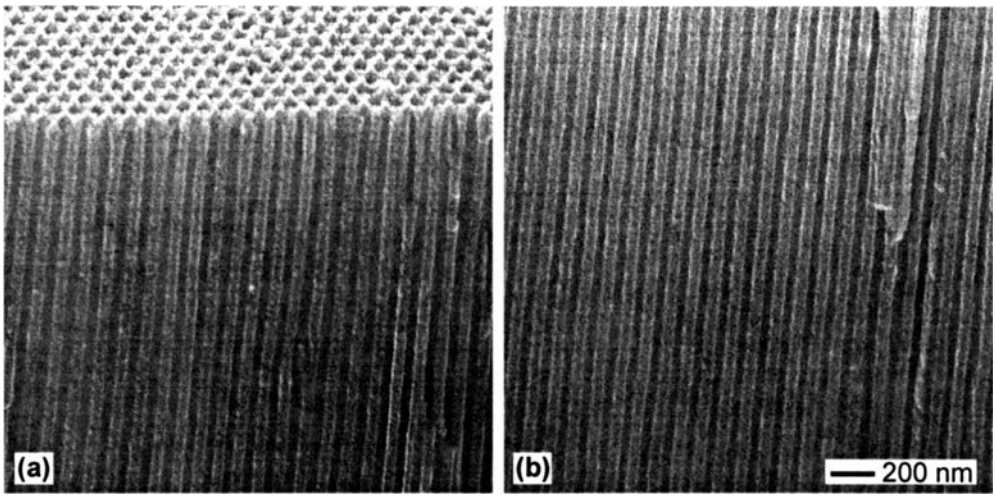

Figure 1. SEM images of cross-section micrograph of the ordered nanopore arrays (courtesy A-P Li).

The magnetism community has been intrigued by the possibility of fabricating magnetic nanowire arrays in self-assembled alumite pores for more than two decades. Much of the early work was concerned with exploratory issues, such as establishing an easy axis for typical preparation conditions and the essential involvement of shape anisotropy, as opposed to magnetocrystalline anisotropy. More recently, attention has shifted towards the understanding of magnetization processes. Particularly interesting problems are the magnetic hysteresis of the wires and the time dependence of the magnetic reversal: it has become well known that simple reversal mechanisms, such as coherent rotation and curling, are unable to account for the observed hysteretic behaviour. For example, the coercivity of the wire arrays is often greatly overestimated by those delocalized reversal modes. One of our aims is to elaborate that this failure originates from the neglect of morphological (real-structural) wire imperfections.

This review focuses on the discussion of the most recent work that is informed by or impinges upon modern theories of magnetization reversal and thermally activated processes. In section 2, we summarize the technique for synthesis and characterization of the arrays, and in section 3 we develop a general theoretical framework for discussing magnetic properties of nanoscale magnets and introduce elementary models for magnetization reversal and thermally activated processes. Section 4 is devoted to experimental results on Fe, Co and Ni nanowire arrays, section 5 analyses the magnetization reversal in the wire arrays and section 6 discusses multilayered nanowires. Finally, section 7 summarizes this work and outlines some possible future developments.

2. Synthesis and characterization

In this section we give a brief description of synthetic and structural characterization methods typically used to fabricate and study self-assembled magnetic nanoarrays. Further details on the electrochemical aspects of the arrays used can be found elsewhere [11, 15].

2.1. Aluminium surface treatment and anodization

The starting material for the fabrication of anodic nanopores, Al (99.998%), is first degreased in 5% NaOH at 60 °C for 30 s and then neutralized in 1:1 water/HNO_3 for several seconds [16]. Alternatively, it can be degreased in acetone and cleaned in a 1:10:20:69 HF:HNO_3:HCl:H_2O solution [17]. The sample is then electropolished, at 40 V for 20 s in a standard electrolyte containing 165 ml of 65% $HClO_4$, 700 ml ethanol, 100 ml 2-butoxyethanol and 137 ml H_2O. The mean roughness of the polished surface is about 3 nm over a 3 μm square area [17].

Anodization is usually conducted under constant cell potential, although it has been claimed [18] that anodizing at constant voltage is not the best procedure because the film thickens too fast due to the large initial current surge. An electropolished aluminium foil serves as an anode and a platinum mesh or an Al sheet as a counter-electrode (cathode). Aqueous sulphuric, oxalic or phosphoric acid is used as electrolyte. Different anodization conditions yield different pore diameters, wire lengths and centre-to-centre spacings. For example, anodizing Al in 15% sulphuric acid at 10 V dc yields pores having a diameter of about 8 nm and an interval distance (centre-to-centre spacing) of around 35 nm, whereas anodization in 3% oxalic acid at 40 V dc yields diameter and spacing increases to about 70 nm and 110 nm, respectively.

During the anodization process, the pores nucleate randomly on the surface with a broad size distribution. However, under specific conditions, highly ordered hexagonal pore arrays are produced. First, it was found that the pre-annealing of Al before anodization is a necessary step to achieve this goal [19]. The Al grain size is 100 to 200 μm after annealing at 500 °C in nitrogen or high vacuum for 3 hours. Second, a two-step anodization process is employed [20]. The Al is first anodized in 3% oxalic acid at 40 V for 15 minutes, resulting a 'textured' surface. Then the formed oxide layer is removed by wet chemical etching in a mixed solution of 0.2 M chromic acid and 0.4 M phosphoric acid at 60 °C. Subsequently, the sample is re-anodized for a longer time (0.5 to 12 h) using the same parameters as in the first step.

The two-step anodization process described in the previous paragraph yields long-range ordered nanopore arrays such as that shown in figures 1 and 2. Figure 2 shows an atomic force microscopy (AFM) top view of an ordered nanopore array. The pores of the anodic alumina can be widened by immersing the samples in 1% phosphoric acid for different lengths of time without changing the centre-to-centre spacing.

2.2. Electro-deposition of magnetic nanowires

After anodization, the nanopores form on top of the Al with one end open and the other end attached to the Al substrate by a thin alumina barrier layer. The barrier layer underneath the pores blocks the dc current because of its large resistance of 10^{10} to 10^{12} Ω cm [21]. To reduce the metal ions and deposit the metal into the pores, the alternating current is therefore imposed between the anodic alumina and the cathode. Since anodic alumina conducts preferentially in only one direction (the cathodic direction), metal ions are reduced inside the pores during the cathodic half-cycles without reoxidizing in the anodic half-cycles [22].

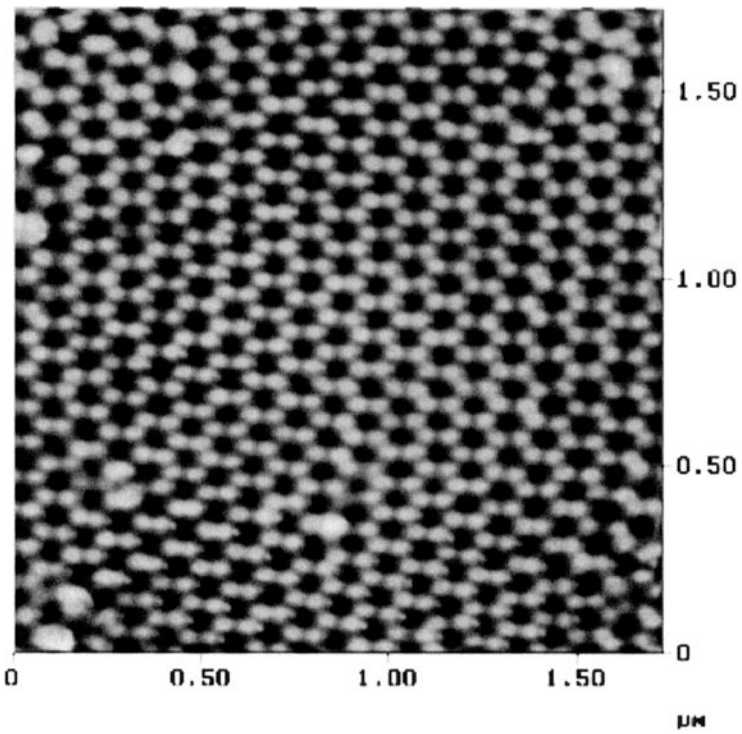

Figure 2. AFM top view of a nanopore array in anodic alumina prepared by three-step anodization. Anodization was conducted in 3% oxalic acid at 40 V.

Magnetic materials, such as Fe, Co, Ni and their alloys, can be easily electro-deposited into the pores using aqueous salt solutions, such as $FeSO_4$ or $CoSO_4$. Typical ac voltages and frequencies are 10–20 V and 50–300 Hz [23]. Boric acid, usually 25–45 g l^{-1} (pH value 3–4), can be added to make the deposition easier. To prevent oxidation of the ferrous material to ferric material, especially when depositing Fe, it is useful to add an inhibitor, such as citric acid or ascorbic acid, to the solution.

When anodizing in oxalic acid at high anodizing voltages (more than 30 V), the barrier layer becomes too thick and prevents the ac electroplating. Usually, the thickness of the barrier layer can be reduced by lowering the dc anodizing voltage to 5 V after the normal anodization, which helps subsequent metal deposition. To avoid oxidation, the pores were sealed by putting the deposited samples into boiling water.

2.3. Structural characterization

To perform AFM, the aluminium and alumina barrier layer are separated from the porous template. This latter is done by dipping the anodized sample into a mixed solution of 0.2 M chromic acid and 0.4 M phosphoric acid for a few hours, depending on the anodizing time. Slightly elevated temperatures, about 60 °C, help to dissolve the alumina barrier layer.

The transmission electron microscopy (TEM) plan-view samples are prepared by standard dimpling and ion milling. The nanowires are released by immersing the specimen in the mixed solution of 0.2 M chromic acid and 0.4 M phosphoric acid and are caught by a carbon grid.

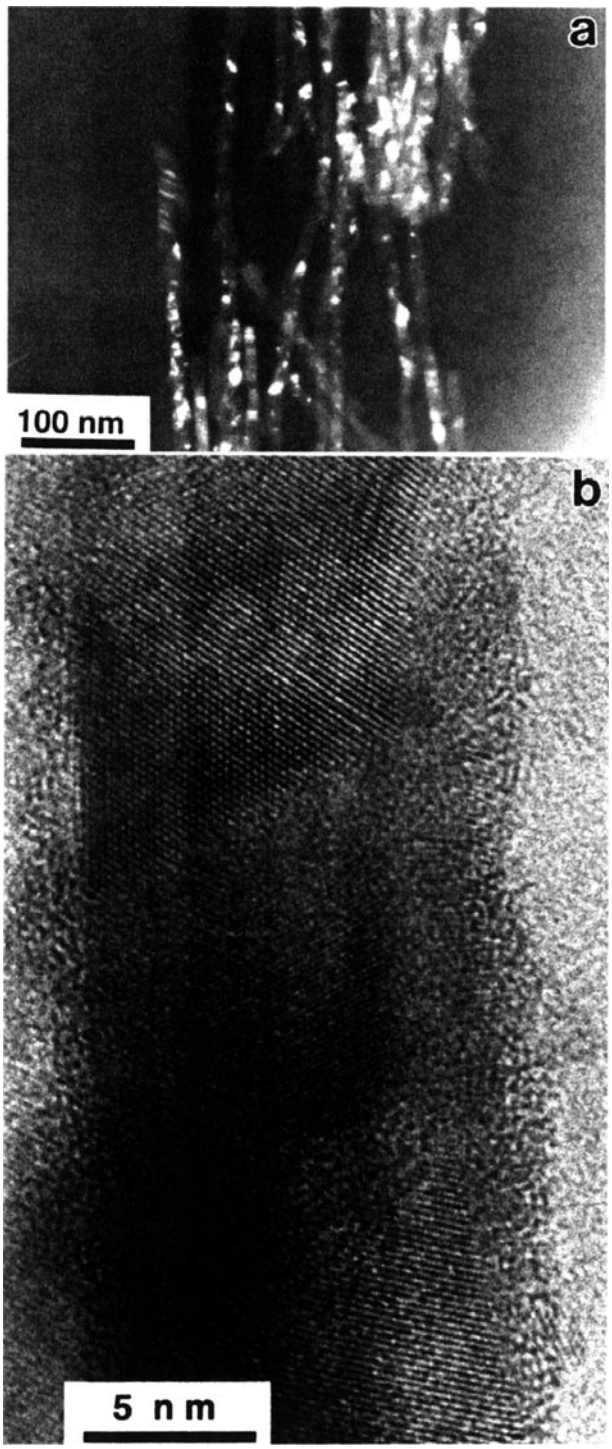

Figure 3. TEM micrographs: (a) Ni nanowires freed from the alumina and (b) single nanowire.

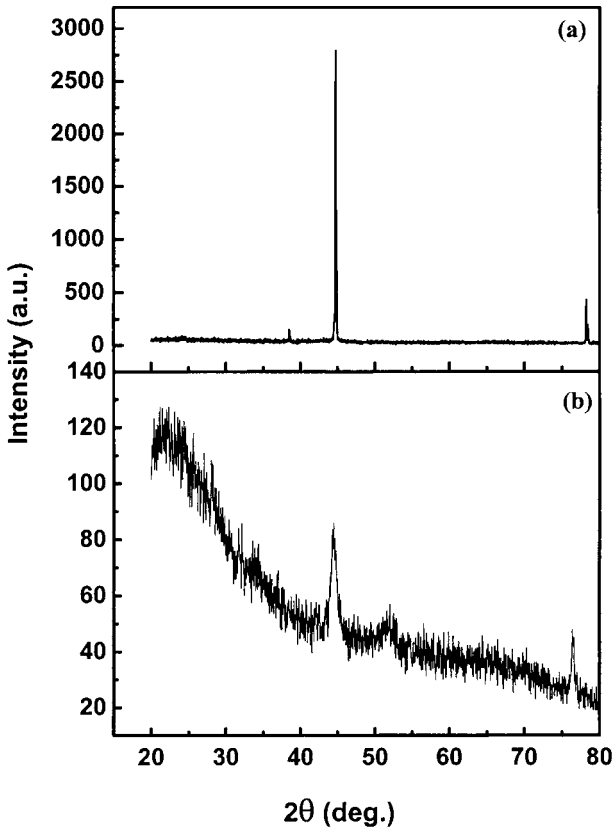

Figure 4. XRD diffraction pattern for Ni nanowire arrays (a) with and (b) without Al substrate.

Figure 3(a) shows the TEM image of Ni nanowires liberated from anodic films; the nanowires are cylindrical with a length of around 1 μm, depending on the deposition time. Figure 3(b) shows a high-resolution TEM image of a single Ni nanowire liberated from the template. Each wire is polycrystalline, consisting of a chain of single-crystalline segments, and the crystallite size is around 10 nm. We also see that the wires' surfaces are not free of defects and inhomogeneities. In section 5 we will see that these imperfections are of great importance for the theoretical explanation of the magnetic behaviour of the arrays.

The size of the crystallites of Fe, Co and Ni nanowires, as well as the crystalline structure of the nanowires depends on deposition conditions such as the pH value of the solutions and the chemical treatment of the as-anodized template before deposition [24, 25]. The crystallite size can be as large as tens of nanometres or as small as 2–3 nm.

Fe nanowires with single-crystallite sizes of around 40 nm along the wire axis have been produced; the crystal structure is bcc. By contrast, the Ni nanowires consist of fcc crystallites and exhibit a grain size of about 10 nm. The nanostructure of Co wires is more complicated. The Co nanowires consist either of mostly hcp grains or fcc grains or a mixture of both. Li and Metzger [15] and Liu [16] found that Fe particles deposited in anodic alumina are essentially single-crystalline.

Electrochemically fabricated nanowires exhibit a length distribution [25]. To narrow the length distribution, a special treatment can be used [26]: the nanowire-containing template is etched in 0.5 M phosphoric/0.2 M chromic acid at 80 °C for about 1 minute, in order to expose

the tips of most of the metal wires, and then mechanically polished with a silica-impregnated cloth to break and remove the wire tips. After exposing the tips of the wires, one can also create electrical contacts by sputtering or evaporating a conductive layer such as gold.

X-ray diffraction (XRD) analysis cannot be used directly to determine the structure of Ni nanowires embedded in alumina, because some of the diffraction peaks of Ni are very close to those of Al and the intensities of the Al peaks from the substrate are much higher than those of Ni. For structural characterization, the specimens were immersed in 3% mercuric chloride ($HgCl_2$) solution and allowed to stand for half an hour at room temperature to strip the oxide. After washing and drying, the structure of the Ni can be measured by XRD. Figure 4 compares the XRD patterns for Ni nanowire arrays with and without Al substrate. The three peaks appearing in figure 4(a) correspond to Al(111) (38.4°), Al(200) (44.7°) and Al(311) (78.2°), whereas those peaks in figure 4(b) correspond to Ni(111), (200) and (220).

3. Conceptual framework for nanoscale magnets

3.1. Static behaviour

The local magnetization $\boldsymbol{M}(\boldsymbol{r})$ of a magnet is determined by the magnetic free energy $F(\boldsymbol{M}(\boldsymbol{r}))$. The *free*-energy character of this functional refers to the atomic origin of magnetism: F can be considered as an energy expressed in terms of temperature-dependent materials constants such as the spontaneous magnetization $M_s = |\boldsymbol{M}(\boldsymbol{r})|$. The magnetization $\boldsymbol{M}(\boldsymbol{r})$ is obtained by tracing local (or global) minima of F as a function of the external magnetic field H. The corresponding magnetization state in a free-energy minimum is the origin of magnetic *hysteresis*. For example, after switching off a sufficiently large magnetic field the magnetization approaches a nonzero remanence M_r, and reducing the volume-averaged magnetization to zero requires a reverse field known as the coercivity H_c. Both static and dynamic magnetization processes reflect the free-energy landscape, but time-dependent magnetization processes involve, in general, jumps over free-energy barriers (section 3.2).

The magnetic free energy F, which is often simply called magnetic energy and denoted by E, consists of four main terms:

$$F = F_{ex} + F_K + F_{ms} + F_H. \tag{1}$$

The *exchange* contribution to the free energy is

$$F_{ex} = \int A[(\nabla m_x)^2 + (\nabla m_y)^2 + (\nabla m_z)^2]\,\mathrm{d}V \tag{2}$$

where A denotes the exchange stiffness and $\boldsymbol{m} = \boldsymbol{M}/M_s$ is the reduced magnetization. The other terms in (1) can be written as integrals over free-energy densities $\eta_i(\boldsymbol{r})$, so that $F_i = \int \eta_i(\boldsymbol{r})\,\mathrm{d}V$. In the following sections, we will encounter a variety of free-energy expressions, but the underlying physics is most easily discussed by considering a uniformly magnetized grain of volume V. The leading second-order *uniaxial anisotropy* contribution is

$$F_K = K_u V \sin^2\theta \tag{3}$$

where K_u is the first anisotropy constant and θ is the angle between $\boldsymbol{M}$ and the easy axis of magnetization. For ellipsoidal grains magnetized along a principal axis, the *magnetostatic self-interaction* can be written as

$$F_{ms} = \tfrac{1}{2} N M_s^2 \tag{4}$$

where $N(M)$ is the demagnetizing factor. This term reflects the magnetostatic dipole interaction of the atomic magnetic moments inside the grain. When the principal axis of an

ellipsoid of revolution is parallel to the easy axis, (4) can be rewritten as a uniaxial anisotropy and is then called *shape anisotropy* [27]. Finally, the magnetostatic interaction of the magnet with the external magnetic field is described by the *Zeeman* term

$$E_H = -H M_s V \cos\phi \tag{5}$$

where ϕ is the angle between the field H and the magnetization.

Equations (3)–(5) are the basis for the simplest model of nanomagnets, the Stoner–Wohlfarth (SW) model [28], which assumes coherent rotation of the magnetization in a grain with uniaxial anisotropy. When the field is applied along the easy axis, the hysteresis loop is rectangular and the coercivity H_c is equal to the anisotropy field

$$H_A = \frac{2K_u}{M_s}. \tag{6}$$

Applying the field perpendicular to the easy axis yields a straight line $M(H)$ which reaches $M = M_s$ at $H = H_A$. For intermediate field directions, $H_c < H_A$. In a variety of cases it is meaningful to approximate a magnet as an ensemble of noninteracting and randomly oriented Stoner–Wohlfarth particles. Averaging over all spatial directions yields a hysteresis loop characterized by $M_r = 0.5\ M_s$ and $H_c = 0.48\ H_A$.

Naturally, a real magnetic material is far more complicated than a collection of independent SW particles. First, interactions between particles may lead to complicated cooperative interparticle effects. Second, in sufficiently large magnetic particles, the magnetization configuration $\boldsymbol{M}(\boldsymbol{r})$ may become nonuniform (incoherent). Nonuniform magnetization states often amount to a reduction of the barriers between neighboring free-energy minima. In fact, equation (1) tends to greatly overestimate the coercivity of real magnets, because it ignores incoherent reversal (section 5.2).

A well known example of a nonuniform magnetization state is *magnetic domains* separated by domain walls whose thickness is of the order of

$$\delta_w = \pi\sqrt{\frac{A}{K_u}}. \tag{7}$$

Domain formation is favourable from the point of view of magnetostatic self-interaction but requires some domain-wall energy. Evaluating the net free-energy gain on domain formation reveals that equilibrium domains are favourable for particles whose diameter exceeds the critical size

$$D_c = \frac{18}{\pi}\frac{\sqrt{AK_u}}{M_s^2}. \tag{8}$$

When several grains or particles in a nanomagnet are coupled together by exchange to form a *magnetic cluster*, the concept of a domain wall is sometimes broadened to include boundaries between these magnetic clusters which are then called 'interaction domains'.

The formation of equilibrium domains, as envisaged by (8), must not be confused with nonuniform (incoherent) magnetization states occurring during magnetization reversal. In perfect and aligned ellipsoids of revolution, such as spheres, 'needles' and 'plates', the reversal starts with a *nucleation* instability of the remanent state. In small particles and thin wires the reversal is uniform (coherent), but in macroscopic ellipsoids it is incoherent [27]. In perfect wires, the transition from coherent to incoherent nucleation occurs at an anisotropy-independent coherence diameter $d_{coh} = 7.31\ l_{ex}$, where $l_{ex} = \sqrt{A/4\pi M_s^2}$ is the *exchange length*. For Fe, Co and Ni, the coherence diameters are about 11, 15 and 25 nm, respectively.

A widely used way of qualitatively gauging weak interactions between ensembles of grains is to use 'delta-m' plots and similar methods such as Henkel, and 'delta-h' plots. These plots

go back to earlier works by Henkel [29] and Wohlfarth [30], who compared different methods of remanence acquisition. For example, Δm is defined as follows:

$$\Delta m(H) = m_d(H) - [1 - 2m_r(H)] \tag{9}$$

where $m_d = M_d/M_r$ is the dc demagnetization remanence divided by the 'ordinary' remanence $M_r = M_r(\infty)$ and $m_r(H) = M_r(H)/M_r(\infty)$ is the reduced isothermal remanence. Δm plots as a function of field tend towards positive or negative bumps near the coercivity H_c. In the limit of weakly interacting grains, these bumps indicate positive ferromagnetic exchange or negative magnetostatic interactions between the grains, respectively. However, (9) is unable to account for cooperative phenomena existing in strongly coupled grains or continuous media, such as domain-wall motion.

The interaction problem is closely related to the demagnetizing-field problem. The demagnetizing field $H_d = -NM$ is often interpreted as an internal-field correction derived from Maxwell's equations, although the validity of this interpretation is limited to macroscopic magnets [31]. For ideal infinite films, $N = 0$ and $H_d = 0$ when the magnetization is in the film plane, but $N = 4\pi$ and $H_d = -4\pi M$ for perpendicular magnetization.

The hysteresis of a magnet is strongly affected by imperfections. On the one hand, imperfections may reduce the free-energy barriers associated with the onset of magnetic reversal (nucleation). On the other hand, defects may inhibit the motion of domains (pinning). A widely used phenomenological expression for the coercivity is [32]

$$H_c = \alpha \frac{2K_u}{M_s} - N_{eff} M_s. \tag{10}$$

Here α is a parameter that depends on grain orientation and reversal mechanism, and N_{eff} is an effective demagnetizing factor which is intended to account for magnetostatic interactions. By means of (10) one can rationalize H_c values of 20–30% of H_A, as often observed.

3.2. Time-dependent behaviour

The above discussion relies on the minimization of the free energy and therefore ignores that thermal fluctuations may cause jumps over energy barriers. Ignoring the destabilizing effect of a reverse magnetic field, we find that typical energy barriers E_B are larger than $k_B T$ by several orders of magnitude, so that the corresponding Boltzmann factor $\exp(-E_B/k_B T)$ is negligibly small. However, an external magnetic field changes the heights of the free-energy minima and barriers, and close to an irreversible jump from one minimum into another minimum the free-energy barrier $E_B(H)$ to be surmounted is very small. In this regime, thermal activation yields experimentally relevant corrections.

There are several time-dependent magnetization phenomena. For a collection of non-interacting grains, the magnetization decays according to [33].

$$M(H, t) = M(H, \infty) + [M(H, 0) - M(H, \infty)] \exp(-t/\tau). \tag{11}$$

Here the *relaxation time* τ is given by

$$1/\tau = f_0 \exp(-E_B(H)/k_B T) \tag{12}$$

where f_0 is an attempt frequency (about 10^9 Hz) [34, 35]. Equation (11) is easily generalized to the case where the free-energy landscape exhibits an energy-barrier distribution $P(E_B(H))$, as is frequently the case due to the random nature of structural imperfections. Averaging (11) over a distribution of energy barriers yields the logarithmic law [27, 33, 36]

$$M(H, t) = M(H, t_0) - S(H) \ln(t/t_0) \tag{13}$$

where $S(H)$ is the *magnetic viscosity*. This equation holds only over an intermediate time range of several decades, and $S(H)$ often exhibits a maximum in a reverse field near H_c.

A complicated problem is the relation between phenomenological equations such as (13) and the real structure of a magnet. For aligned and non-interacting SW grains, equations (1) to (5) can be used to show that

$$E_B(H) = K_u V \left(1 - \frac{H}{H_A}\right)^m \tag{14}$$

where $m = 2$ and K_u includes the particles' shape anisotropy. More generally, the exponent m is 3/2 or 2 for a variety of pinning and nucleation models, depending on the symmetry of the energy landscape [27, 36].

Equation (14) shows that free-energy barriers decrease with the particle size. When $K_u V$ is comparable to $k_B T$ the magnetization decays very rapidly, which is known as *superparamagnetism*. In more detail, defining superparamagnetism by $\tau = 100$ s leads to the stability condition

$$\frac{K_u V}{k_B T} \geqslant 25 \tag{15}$$

where $K_u V / k_B T \equiv \xi$ is referred to as the stability parameter. For a grain to be stable for 10 years (3×10^8 s), $\xi \geqslant 40$. On the other hand, the magnetization of a grain of volume $V = (5\,\mathrm{nm})^3$ and anisotropy $K_u = 4 \times 10^6$ erg cm^{-3} is thermally unstable at room temperature, because $\xi = 12$.

Since τ is the time necessary to jump over the free-energy barrier, equation (12) can, in good approximation, be considered as an implicit relation for the coercivity

$$E_B(H_c) = k_B T \ln(f_0 \tau). \tag{16}$$

Here τ is the characteristic time scale of the coercivity measurement. Combining (12) and (14) yields [27, 37]

$$H_c = H_A \left(1 - \left(\frac{k_B T}{K_u V} \ln(f_0 \tau)\right)^{1/m}\right). \tag{17}$$

Improving on (16) by a master-equation approach yields a relatively unimportant factor of $\ln 2 = 0.693$ [37], which is usually incorporated into f_0.

In practice, τ is tuned by varying the *sweep rate* $\eta = \mathrm{d}H/\mathrm{d}t \sim 1/\tau$. An experimental approach to analyse the resulting sweep-rate dependence of the coercivity is to exploit the linear relation [27, 38]

$$H_c(\eta) = H_c(\eta_0) + \frac{k_B T}{M_s V^*} \ln\left(\frac{\eta}{\eta_0}\right) \tag{18}$$

which defines an *activation volume* V^*. Linearizing (17) with respect to $\ln(\tau/\eta_0) = -\ln(\tau/t\eta_0)$ and comparing the result with (18) yields [27]

$$V^* = \frac{m}{2} \left(\frac{25 k_B T}{K_u V}\right)^{1/m} V. \tag{19}$$

This equation shows that the activation volume V^* is only loosely related to the 'physical' volume V. An alternative method to derive (19) is to start from the expression [35, 39–41]

$$V^* = -\frac{1}{M_s} \frac{\partial E_B(H)}{\partial H}\bigg|_{H_c(T,V)} \tag{20}$$

where H_c is obtained by solving $E_B(H_c) = 25 k_B T$ and E_B is given by (13).

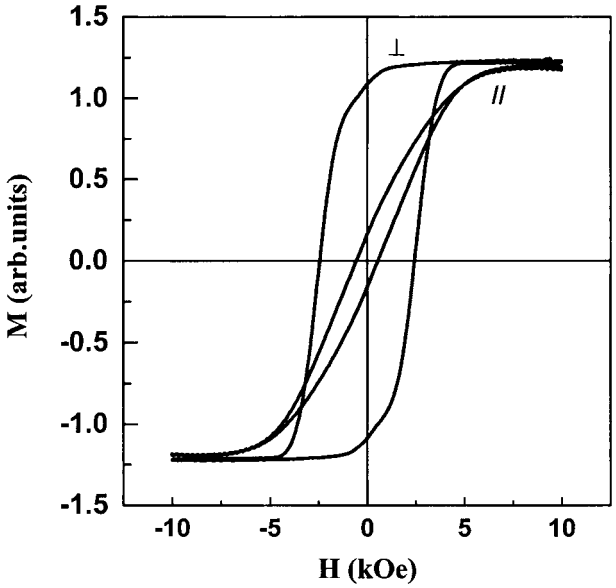

Figure 5. Typical magnetic hysteresis loops for Fe nanowire arrays. The field is applied along and perpendicular to the wire axis. The mean diameter of the nanowire is about 10 nm.

For $m = 2$, the activation volume (19) can also be written as $V^* = V(1 - H_c/H_A)$. Note that V^* contains two types of temperature dependence: an intrinsic temperature dependence via $K_u(T)$ [27], and an extrinsic temperature dependence via the term $T^{1/m}$ in (19). This distinction is important when one considers materials where the anisotropy is strongly temperature dependent, as it is the case for Ni. The relation between V^* and S is [35, 39, 40]

$$V^* = \frac{k_B T}{M_s S} \chi_{irr} \tag{21}$$

where $\chi_{irr} = \mathrm{d}M_d/\mathrm{d}H$ is the irreversible susceptibility. Both S and χ_{irr} generally have peaks near H_c, so that $V^*(H_c)$ often is determined only at the single field value where the reversal is most significant. Since the irreversible susceptibility translates field variations into magnetization changes, S values determined from magnetic-viscosity experiments generally agree fairly well with sweep-rate values of S.

4. Fe, Co and Ni nanowire arrays

4.1. Fe nanowires

Magnetic properties of Fe nanowires have been studied by a number of groups [15, 22, 23]. Typical sizes range from 10 to 100 nm in diameter and from 0.1 and 1 μm in length. Figure 5 shows hysteresis loops for wires having a diameter of 9 nm and a length of 1 μm; the field is applied parallel and perpendicular to the wire axis. When the field is parallel to the wire axis (perpendicular to the film plane), the coercivity is about 2300 Oe (remanence ratio $M_r/M_s = 0.96$), whereas the coercivity measured perpendicular to the wire axis (in the film plane) is about 300 Oe (remanence ratio 0.055). This indicates that the wires possess uniaxial anisotropy with the easy axis along the wire axis. The perpendicular anisotropy arises mainly from the shape anisotropy of the wires. This phenomenon is often seen in magnets whose shapes can be approximated as thin cylinders or needles. The coercivity measured

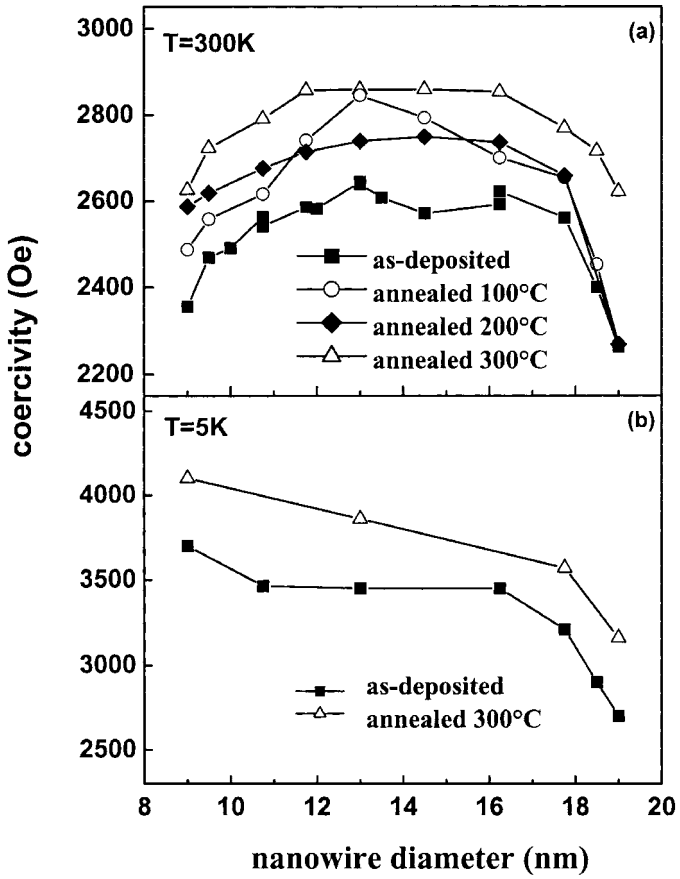

Figure 6. Coercivity H_c of Fe nanowires: (a) H_c as a function of wire diameter for as-deposited and annealed samples, and (b) diameter dependence at 5 K and 300 K.

along the wire axis is 2100–2700 Oe for Fe [22, 23, 42], as compared to 1100–2400 Oe for Co [24, 41–45] and 400–950 Oe for Ni [46–49].

As mentioned above, one can increase the diameter of the pores by soaking the anodized film in phosphoric acid. The diameter is then controlled by the soaking time: varying from 9 to 19 nm for pore-widening times from 0 to 30 minutes [5]. The variation of the coercivity as a function of pore diameter is shown in figure 6(a). H_c increases with increasing diameter until a maximum is reached at about 13 nm. The largest coercivity measured by our group is 2640 Oe for a diameter of 13 nm. Moskovits *et al* [22] and Li [15] reported maximum values of 2220 Oe and 2240 Oe, respectively, both obtained for sulphuric-acid-anodized templates. The dependence of H_c on the wire diameter shows that it is possible to control the magnetic properties of the wires by controlling the fabrication parameters.

Figure 6(b) shows the low-temperature coercivity ($T = 5$ K) as a function of wire diameter for as-deposited and annealed samples. Unlike the maximum seen at 300 K, the coercivity at 5 K decreases continuously with increasing diameter. For the smallest sample (9 nm diameter), the low-temperature coercivity is 3700 Oe, as compared to 2341 Oe at room temperature. For samples with larger diameters, the difference is less pronounced. For example, for a diameter of about 16 nm, the coercivity rises from 2600 Oe at 4 K to 3450 Oe at room temperature.

Some Fe samples were annealed in an attempt to cause grain growth and thus to influence

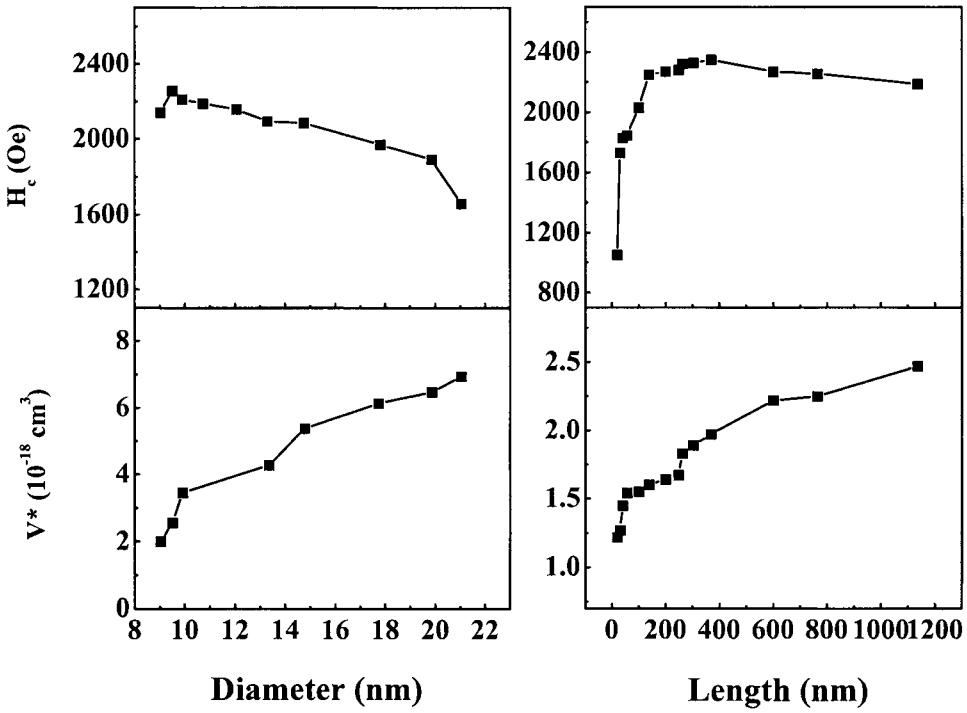

Figure 7. Dependence of coercivity H_c and thermal activation volume V^* of Co wires on wire diameter d_w and length l_w.

the coercivity. They were annealed at 10^{-7} Torr for about 6 hours at different temperatures: 100 °C, 200 °C, 300 °C and 400 °C. Annealing at 100 °C, 200 °C and 300 °C enhances the coercivity for all wires (figure 6). The most pronounced increase is obtained for 300 °C annealing: the value of the coercivity for the sample with diameter of 13 nm increases to 2900 Oe. Annealing at even higher temperatures (400 °C) causes the coercivity drop to about 50 Oe, suggesting that the nanostructures were destroyed or oxidized. The oxidation is probably caused by the ions involved in the deposition process [50].

The coercivity also depends on the aspect ratio, l_w/d_w (wire length divided by wire diameter) [15]. It increases gradually with increasing aspect ratio, but increases very little when the aspect ratio is larger than 10:1 [15]. A likely explanation of this behaviour will be given in section 5. AlMawlawi and his co-workers studied the coercivity of Fe nanowires deposited into oxalic-acid-anodized alumites as a function of deposition time, pore-widening time and anodizing voltage [26]. They found that the coercivity depends strongly on the aspect ratio and only weakly on the pore density (anodizing voltage). H_c decreases as the widening time increases, which is in agreement with our results [23].

4.2. Co nanowires

Typical hysteresis loops for Co nanowires in an anodic alumina template, with aspect ratios greater than 20, are similar to those of Fe nanowires (figure 5). The coercivity measured in the perpendicular direction is as high as 2.6 kOe, whereas the remanence ratio exceeds 0.9 [43]. Figure 7 shows coercivity and thermal activation volume as a function of the nanowire diameter (d_w) and length (l_w). For samples with varying length, d_w is fixed at 10 nm, while

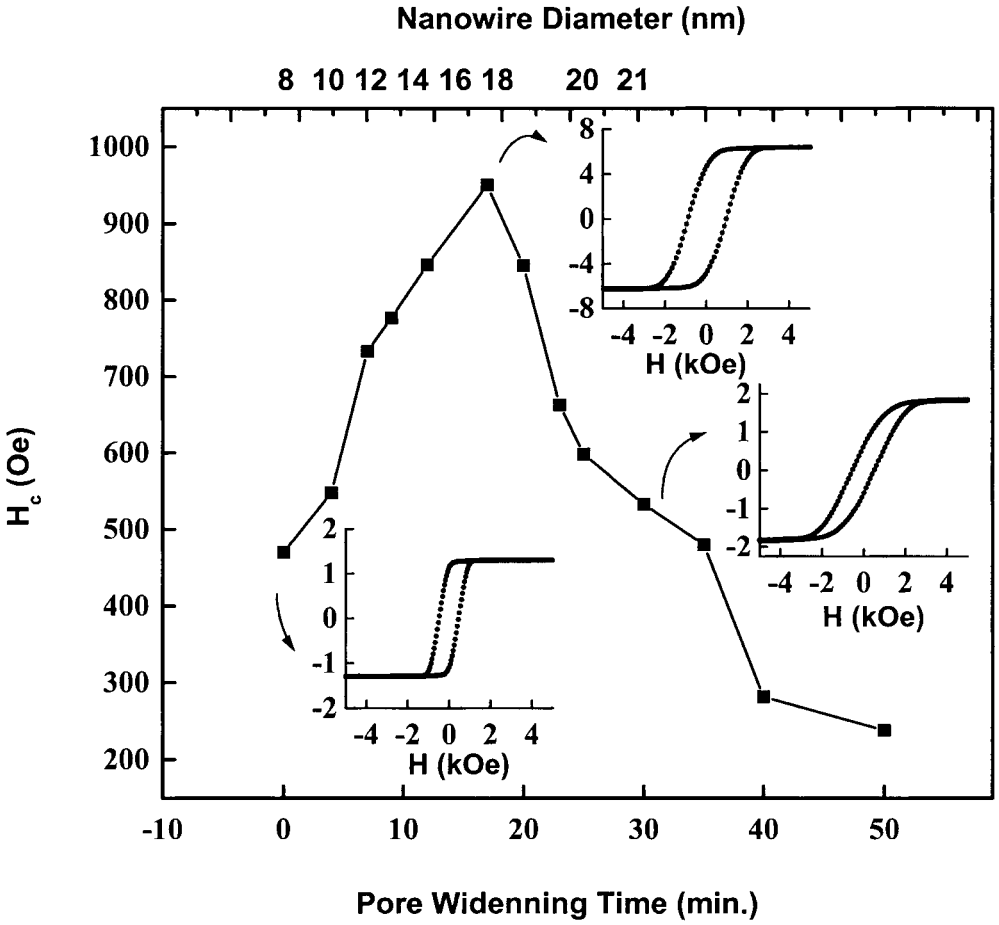

Figure 8. Dependence of the coercivity on the pore-widening time, which determines the nanowire diameter. The corresponding hysteresis loops for Ni nanowires with diameter of 8, 18 and 21 nm are shown as insets.

l_w changes from 10 nm to 1000 nm. On the other hand, for samples with varying diameter, the centre-to-centre distance d_c is fixed at 40 nm and l_w is between 500 nm and 1000 nm, while d_w changes from 9 nm to 20 nm. (This ensures that the aspect ratio remains larger than 25.) The thermal activation volume is used to investigate the energy barriers responsible for the magnetization reversal mechanism. V^* has been determined by exploiting the sweep-rate dependence of coercivity and magnetic viscosity measurements. Since the results obtained by these two methods agree fairly well, only the easier-to-measure sweep-rate activation volumes are shown.

With increasing nanowire length, H_c increases steeply until a constant value of about 2300 Oe is approached, at a length of about 200 nm. V^* increases first rapidly but then gradually with l_w, but it is generally much smaller than the physical wire volumes. This indicates that the magnetization reversal starts in a small region of wires (section 5). With increasing wire diameter, the coercivity gradually decreases.

4.3. Ni nanowires

Figure 8 shows the coercivity as a function of pore widening time, i.e. as a function of the wire diameter [48]. In this measurement, the coercivity is measured with the magnetic field applied along the wire axis. The corresponding hysteresis loops for Ni nanowires with diameters of 8, 18 and 21 nm are shown as insets. Like the Fe and Co wires, the Ni nanowires have easy axes along the wire axis due to the shape anisotropy. For Ni nanowires deposited into an as-anodized template, the coercivity is about 480 Oe. The coercivity increases with pore-widening time and reaches a maximum of 950 Oe for Ni deposited into a template which had been pore-widened for 17 minutes. (The wire diameter is about 18 nm and the spacing is 35 nm). The coercivity then decreases on further increasing the pore diameter. The remanence ratios, M_r/M_s, for these three samples are 0.77, 0.84 and 0.33 respectively.

4.4. Comparison of Fe, Co and Ni

Table 1 compares some magnetic properties of Fe, Co and Ni nanowires. All arrays discussed in this study have aspect ratios larger than 50, exhibit an easy axis along the wire axis and have remanence ratios larger than 0.9. As a first approximation, we can therefore assume that the magnetism of the wires is governed by shape anisotropy. The shape anisotropy field for an infinite cylinder is $2\pi M_s$, where M_s is saturation magnetization. M_s at room temperature is 1707, 1400 and 485 emu cm^{-3} for bulk Fe, Co and Ni, respectively. The corresponding H_A values calculated are 11 000, 8800 and 3400 Oe, respectively. The effective perpendicular anisotropy fields measured by extrapolating magnetization curves are 10 000, 7500 and 3000 Oe, respectively, which are smaller but fairly close to the theoretical limit H_A (table 1). However, due to mechanisms discussed in section 5.2, only a fraction of this value is actually realized as coercivity. The maximum coercivity values achieved at room temperature for Fe, Co and Ni nanowire arrays are 3000 [23], 2600 [43] and 950 [48] Oe, respectively.

Table 1. Some properties of Fe, Co and Ni nanowires (RT = 300 K).

	Fe	Co	Ni	Unit
M_s	1707	1400	485	emu cm^{-3}
$\delta_0 = \delta_w/\pi$	13	4	26	nm
d_{coh}	11	15	25	nm
$2\pi M_s$	10 730	8800	3047	Oe[a]
H_A	10 000	7500	3000	Oe
H_c(RT)	3000	2600	950	Oe
H_c/H_A	0.30	0.35	0.32	1
M_r/M_s	0.93	0.91	0.90	1
$V^*(H_c, \mathrm{RT})$	1.5	2.1	6.0	10^{-18} cm^3

[a] M_s and $2\pi M_s$ have different units in the Gaussian system.

Figure 9 shows the temperature dependence of coercivity. Previous works on Fe nanowires reported a nearly linear dependence of H_c on temperature [51, 52], but figure 9 reveals that there is some curvature. The activation volume V^* has been measured and compared for a variety of Fe, Co and Ni nanowires. The dimensions remain the same as described above. V^* approaches a constant value when the aspect ratio is large. A similar behaviour was also found for Fe nanowires [16]. Table 1 shows typical maximum V^* values for Fe, Co and Ni. To explain and discuss these data, it will be necessary to go beyond Stoner–Wohlfarth-type single-particle V^* models (section 5).

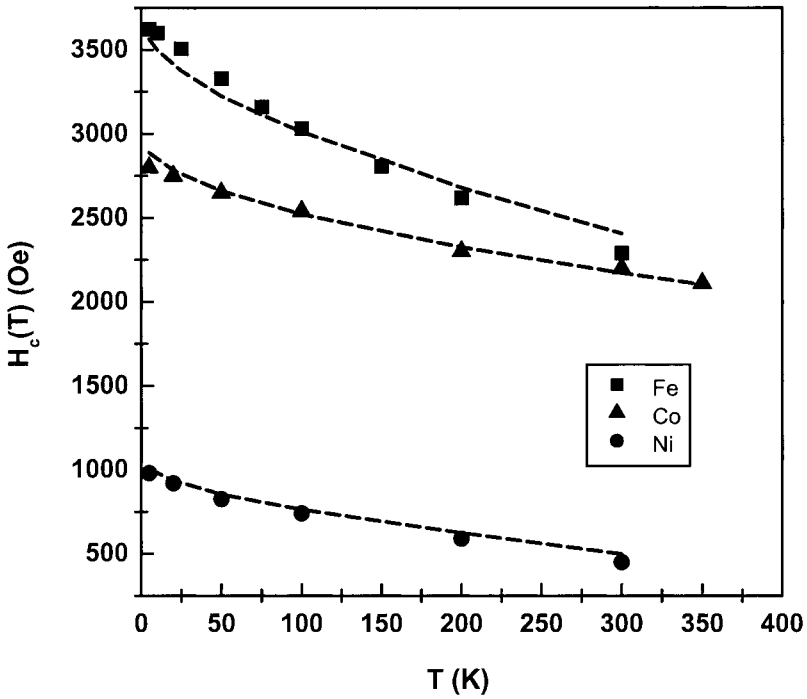

Figure 9. H_c as a function of temperature for Fe, Co and Ni nanowires. The curves are a fit to a phenomenological extension of (17). (Courtesy H Zeng.)

5. Magnetization reversal

The explanation and prediction of hysteresis loops is a key problem in fundamental and applied magnetism. The simplest approach is to model the wires as thin and homogeneous prolate ellipsoids of revolution (needles), for which the Stoner–Wohlfarth theory (section 3.1) predicts rectangular hysteresis loops whose coercivity is equal to H_A. However, it has been known for decades that neither the coercivity nor the loop shape of real materials is reproduced by the SW theory. There are two main reasons: (i) the size of the particles (the diameter of the wires) is often much larger than the coherence length (section 3.1) and (ii) real particles (real wires) contain various kinds of imperfection. Furthermore, we have to consider the influence of magnetostatic interactions between wires.

The incoherent nucleation in perfect ellipsoids of revolution is realized by magnetization curling [27, 53]. Curling means that the nucleation of reverse domains in thick wires is facilitated by magnetostatic flux closure [31]. However, the diameter d_c of the wires considered here is smaller than the coherence length l_{coh} (section 3.1), so that the curling mode is suppressed by interatomic exchange and the modelling of the wires is somewhat facilitated.

5.1. Magnetostatic interactions between wires

The alumina template is not able to mediate exchange interactions over more than a few interatomic distances, so that interactions between the wires are realized by magnetostatic dipole interactions [43]. The description of individual wires in terms of shape anisotropy is questionable (section 5.2), but in fair approximation we can describe the effect of neighbouring

wires as an effective-field correction $\Delta H = -\Delta N M$ [43]. This demagnetizing-field correction gives rise to a skewing (shearing) of the loop.

Based on the crude assumption that the slope $\mathrm{d}M/\mathrm{d}H$ at H_c is infinite for non-interacting and well aligned nanowires, ΔN has been determined experimentally. As shown in figure 10, ΔN increases with packing density $P = (d_w/d_c)^2/2\sqrt{3}$, where d_w is the wire diameter and d_c is the centre-to-centre spacing of the hexagonal arrays. In figure 10, a slope of 10.6 is obtained from the linear fitting of ΔN as a function of P, which is very close to the theoretical prediction $\Delta N = 4\pi P$ obtained by magnetostatic calculation [43].

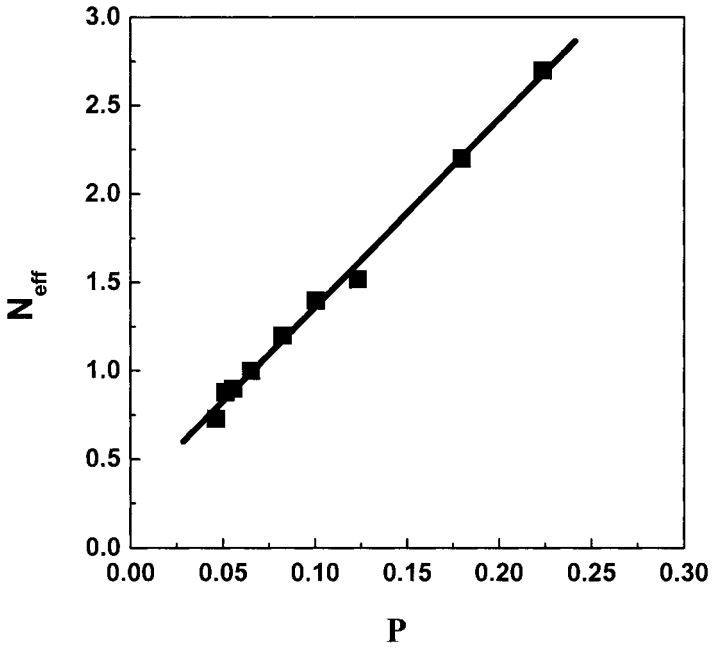

Figure 10. Dependence of demagnetizing-factor correction ΔN as a function of packing density P for Co nanowires.

The ultimate criterion for the applicability of the demagnetizing-field approximation is that the wires switch independently of each other, so that the effect of neighbouring wires can be described as an external-field correction. This is usually the case for weak interactions. As analysed in a different context [54], strong interactions mean that the wires switch cooperatively, so that the picture of an effective demagnetizing field needs to be modified.

5.2. Localized and delocalized nucleation modes

As mentioned in section 3.1, the Stoner–Wohlfarth theory fails to describe the hysteresis of the nanowires. In particular, the coercivity of the wires is overestimated by a factor of the order of three (table 1), and measured activation volumes are often much smaller than the wire volume. For example, using a magnetic force microscope (MFM) with an *in situ* electromagnet, Schultz and coworkers have studied the magnetization reversal of single Ni nanowires [55]. By measuring the angular dependence of the switching field for cylindrical Ni wires ranging from $R = 20$ nm to $R = 500$ nm, the authors found that, except for a narrow range of radii where the angular dependence is consistent with the curling mode, the switching-field data are inconsistent with analytical solutions such as curling in an infinite cylinder or coherent

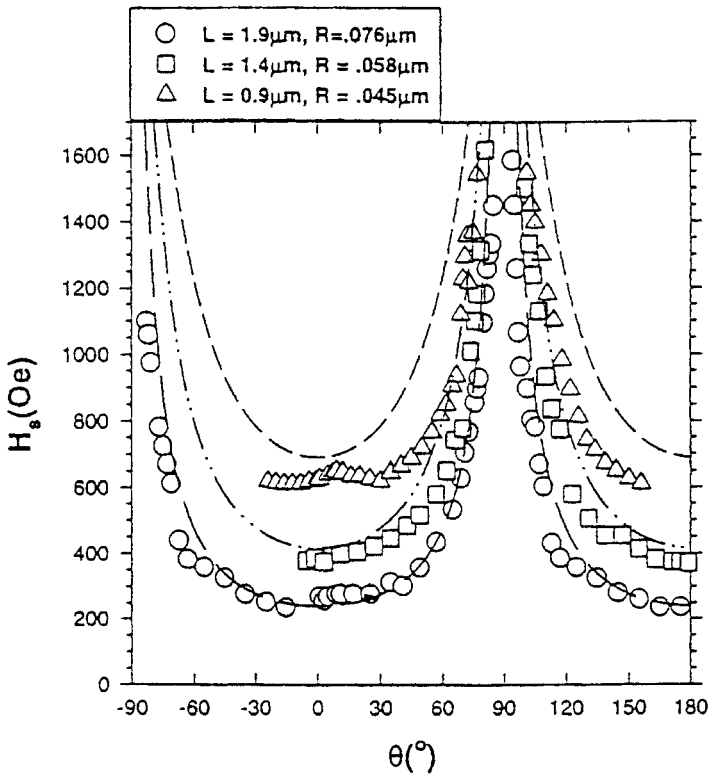

Figure 11. Switching field (nucleation field) against angle between applied field and the long axis for Ni wires with different aspect ratios. The dashed curves correspond to $H_n(\theta)$ for nucleation by curling for infinite cylinders with diameters equal to those of wires (after R O'Barr and S Schultz).

rotation in an elongated ellipsoid. Figure 11 shows the angular dependence of saturation field, H_s, for Ni columns with different aspect ratios. The dashed lines correspond to the nucleation field H_n for curling in infinite cylinders with the same diameter as these columns. Similarly, Wegrowe *et al* [56] found that their magnetization data could be fitted to the curling prediction only with the paradoxical assumption that the shape of the 'infinite cylinder' is like a rugby ball, with an aspect ratio of the order of 2:1.

The failure of the Stoner–Wohlfarth theory, which is also observed in bulk magnets [27], has its main origin in the *localization* of the magnetic reversal [27, 31, 57]. The coherent-rotation and curling modes are delocalized, that is, they extend throughout the wire. Localized reversal, which starts in a very small region of a magnet, involves very inhomogeneous magnetization states and is therefore unfavourable from the point of view of interatomic exchange. However, magnetization processes localized in the vicinity of imperfections may be favourable due to locally reduced anisotropy and magnetostatic energies. This localization mechanism is, in fact, well established for a variety of magnetic materials and explains Brown's paradox that α in (10) is almost inevitably smaller than predicted from the corresponding delocalized mode ($\alpha \ll 1$ in many materials).

Since the delocalized coherent-rotation and curling modes are exact solutions of the nucleation problem in homogeneous ellipsoids of revolution [27, 31, 53], we must consider deviations from the ideal of homogeneous ellipsoids of revolution, for example structural inhomogeneities and irregular features at the wire ends. Thermal activation may, in principle,

create a localized nucleus, but due to the small Boltzmann factor $\exp(-E_B/k_BT)$ this is an extremely unlikely event (figure 12). In fact, thermal excitations are observed as magnetic-viscosity corrections (section 3.2). Figure 13 gives a schematic idea of how the magnetization of a localized unit (dark area) reverses. The reason for the localization is that wires are, at least to some degree, polycrystalline [24, 43], and even in nearly single-crystalline wires there are small magnetization perturbances associated with wire-thickness fluctuations, crystalline defects, impurities and geometrical features at the wire ends.

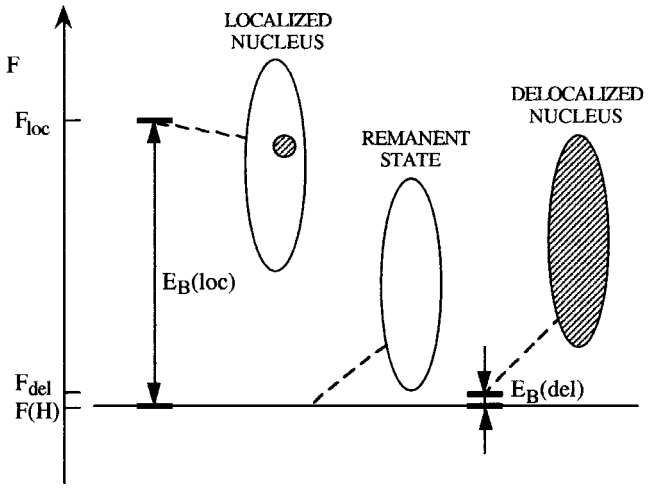

Figure 12. Energy barriers in a *perfect* ellipsoid of revolution. $F(H)$ is the free energy of the metastable minimum, whereas F_{loc} and F_{del} are the saddle-point free energies for delocalized and localized nucleation, respectively. To initiate magnetic reversal one can (i) increase $F(H)$ by increasing the reverse magnetic field and (ii) wait until thermal activation over energy barriers occurs. Due to the pronounced Boltzmann factor, $\exp(-E_B/k_BT)$, the thermally activated creation of a localized nucleus is extremely unlikely. (It may be likely when $F(H) > F_{del}$, but this occurs after having reached the 'static' reversal condition $E_B(\text{del}) = 0$.) In imperfect wires there are often localized nuclei characterized by $F_{loc} < F_{del}$, so the localized reversal is more likely. For the relatively unimportant difference between energy barriers and free-energy barriers see [74].

5.3. Nearly perfect wires

From the electron-localization analogy [58] it follows that an arbitrarily weak inhomogeneity leads to a localization of the nucleation mode in one dimension. In this subsection we use an exactly solvable model to show how small inhomogeneities lead to magnetic localization and calculate both the localization length [47] and the coercivity. The wire is modelled as an infinitely long but very thin wire ($d_w < d_{coh}$), and the inhomogeneity consists in a local reduction of the first anisotropy constant $K_u(z)$. In other words, due to soft-magnetic impurities or defects a small part of the wire is slightly softer than the remaining part of the wire. The free energy (1) of a very thin wire can be written as

$$F = \int [A(\nabla \boldsymbol{s})^2 - K_{eff}(\boldsymbol{n} \cdot \boldsymbol{s})^2 - M_s \boldsymbol{H} \cdot \boldsymbol{s}] \, \mathrm{d}V \tag{22}$$

where $\boldsymbol{s} = \boldsymbol{M}/M_s$ and the unit vector $\boldsymbol{n} = \boldsymbol{n}(\boldsymbol{r})$ denotes the generally random local easy axis. The effective anisotropy constant $K_{eff} = K_u(\boldsymbol{r}) + M_s^2/2$ incorporates magnetostatic shape, magnetocrystalline and magneto-elastic anisotropy contributions [47].

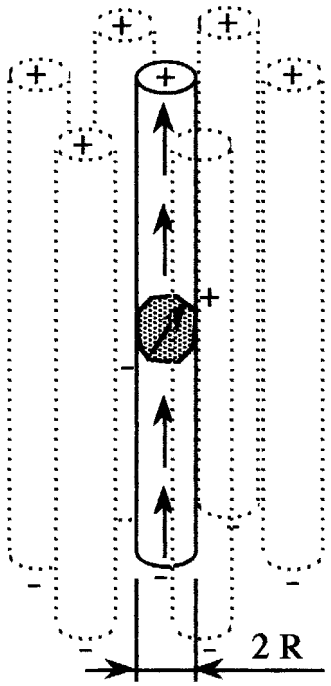

Figure 13. Schematic view of hexagonal array of magnetic nanowires deposited in alumina. The arrows give the local magnetization direction, whereas the + and − signs denote the corresponding magnetic charges. The magnetic field is parallel to the wires.

Putting $\boldsymbol{n} = \boldsymbol{e}_z$ and $K_u(\boldsymbol{r}) = K_u(z)$ in (22) yields

$$F = \frac{\pi}{4} d_w^2 \int \left(A \left(\frac{\partial \phi}{\partial z} \right)^2 + (K_{eff}(z) + \tfrac{1}{2} M_s H) \phi^2 \right) \mathrm{d}z. \tag{23}$$

Here $\phi(z)$ is the angle between the wire axis (z-axis) and the local magnetization and $H = H_z$ is the external magnetic field. In the standard way, the nucleation mode $\phi_N(z)$ is obtained by minimizing (23) and solving the resulting eigenvalue problem. Figure 14 shows the nucleation mode for a small inhomogeneity of length L and reduced anisotropy K_s ($K_{eff} = K_0$ for $|z| > L/2$ and $K_{eff} = K_s$ for $|z| < L/2$). The mode decays as $\exp(-z/R)$, where the localization or decay length is given by

$$R = \frac{2A}{(K_0 - K_s)L}. \tag{24}$$

The localization of the nucleation mode is accompanied by a coercivity reduction:

$$H_c = H_A - \frac{(K_0 - K_s)^2 L^2}{2AM_s}. \tag{25}$$

Equations (24) and (25) are restricted to small perturbations, but it can be shown that, for arbitrary L, the coercivity obeys $H_c = H_A - 2A/(M_s R^2)$. For example, the assumption that a piece of a Co wire (length $L = 4$ nm) is magnetically soft yields $R = 11$ nm and a coercivity reduction of 18%. It can be shown that the localized nucleus corresponds to $m = 2$ (section 3.2), and the corresponding activation volume $V^* = \pi d_w^2 (L + 2R)/4$.

The result (24) confirms our starting conjecture that any arbitrarily small disorder gives rise to localization and shows that the actual degree of localization (the localization length) is

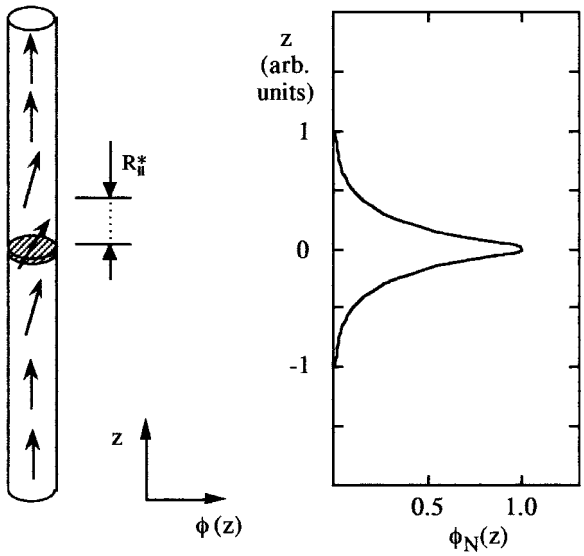

Figure 14. Nucleation-mode localization in a nearly single-crystalline wire. The length of the perturbed wire region (dashed area) is L. After nucleation, the magnetization reversal proceeds by the propagation of two domain walls.

strongly dependent on the wire's nanostructure. For zero disorder, the localization length goes to infinity and the reversal degenerates into coherent rotation. The coercivity reduction (25) is indeed observed in real wires [43, 45] and bulk magnets [27, 57], although the model (23) is too simple to reproduce experimental coercivity data quantitatively.

5.4. Activation volume and temperature dependence of coercivity

Equation (19), where $m > 1$, predicts that the activation volume V^* diverges for $V \to \infty$. As discussed in section 5.2, this divergence is not observed in reality. To analyse this problem [47] we consider the wire as coherently reversing long ellipsoids of revolution (wire length $l_w \gg d_w$), so that $N \approx 2\pi$ perpendicular to the wire axis. Figure 15 compares the V^* and H_c predictions (19) and (17), respectively, with experimental data; the fitting parameters are V and K. Since V^* is proportional to $\sqrt{V}$ and $V \approx \pi d_w^2 l_w/4$, (19) predicts a square-root dependence of V^* on the wire length l_w. Figure 15(a) shows that the square-root prediction (dashed lines) works fairly well for short wires but breaks down above a critical length. This confirms our above finding: when the wire length exceeds a critical value of the order of R then the physical volume V (and the activation volume V^*) remain largely unchanged. Summarizing, in terms of figure 13 the micromagnetic localization is realized by prolate regions whose aspect ratio depends on the real structure of the wires but is, in general, significantly larger than one.

Figure 15(b) compares the coercivity prediction with the experimental dependence of the coercivity of Co on the wire length L. The slight deterioration of the coercivity of very long wires is reminiscent of the finite-size behaviour of bulk and thin-film magnets and means [27] that large magnets are more likely to contain pronounced inhomogeneities harmful to coercivity. For a discussion of figure 15 and of the involved parameters see [47].

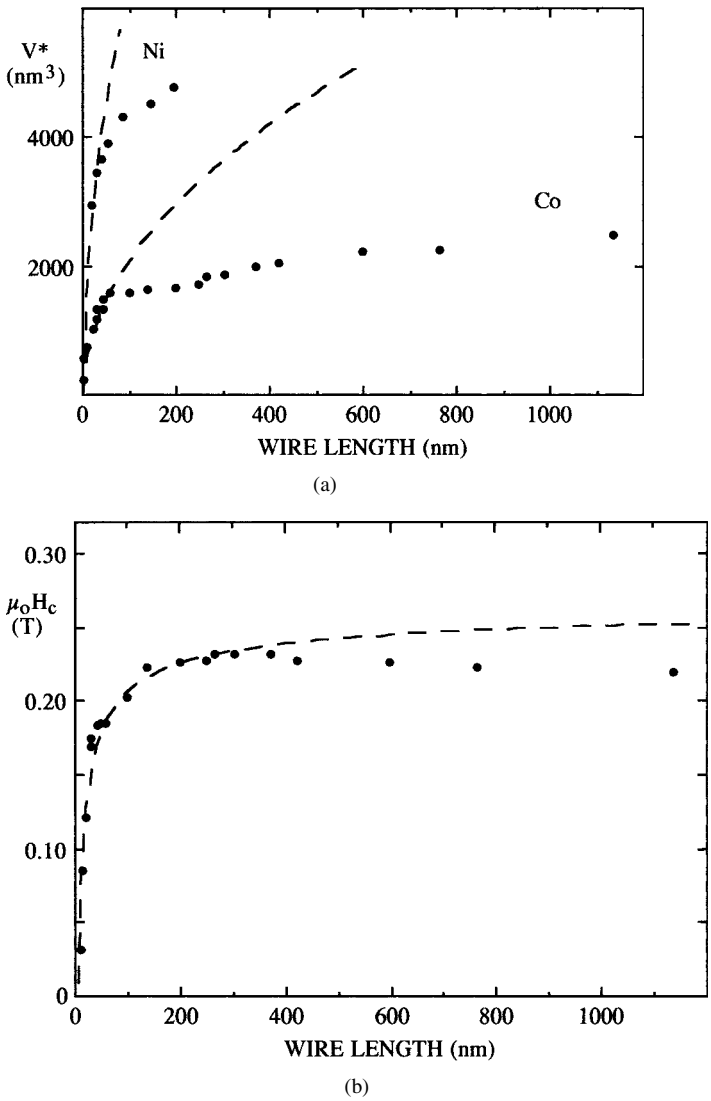

Figure 15. Wire-length dependence of hysteretic properties: (a) thermal activation volume of Co and Ni nanowires and (b) coercivity of Co nanowires. The experimental data refer to wires whose lengths have been modified by changing the deposition conditions (time and voltage). The wire radii are 5.5 and 10 nm for Co [17] and Ni [20], respectively. The dashed lines are theoretical predictions based on the assumption that the physical activation volume is proportional to the wire length.

5.5. Polycrystallinity

The polycrystallinity of the wires and the rough wire surface (figure 3) mean that the local easy axis $\boldsymbol{n}(\boldsymbol{r})$ is a random quantity. This randomness affects both the magnetic ground state and the hysteresis loop. In particular, it gives rise to deviations from the rectangular loop shape predicted for aligned Stoner–Wohlfarth particles. Random-field [59] and random-anisotropy phenomena have attracted much attention in the past due to their interesting dimensional dependence [60–64]. Essentially, the random preferential magnetization directions of the

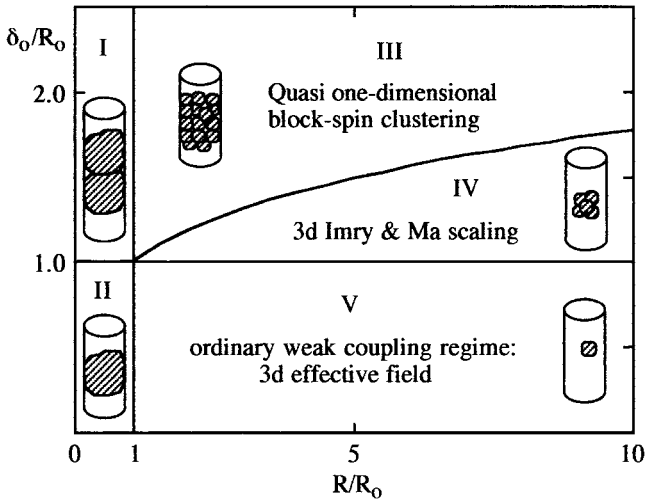

Figure 16. Magnetic phase diagram for polycrystalline wires. The regions are (I) truly one dimensional and cooperative, (II) truly one dimensional and non-cooperative, (III) quasi-one-dimensional cooperative, (IV) three dimensional cooperative, and (V) three dimensional non-cooperative.

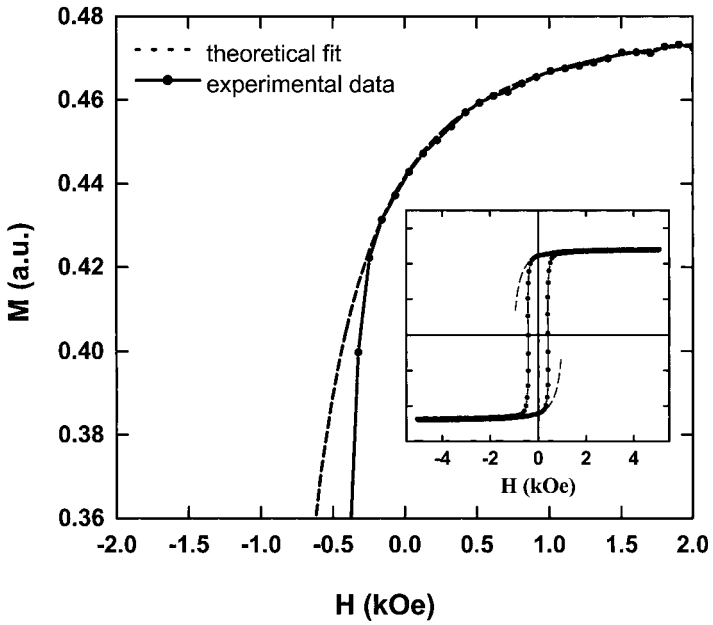

Figure 17. Theoretical fit for hysteresis loop of Ni nanowire arrays. The inset indicates that the theory overestimates the coercivity.

crystallites favour magnetization misalignment but must compete against the exchange and external fields, which favour magnetization alignment.

In this subsection, we discuss one-dimensional random-anisotropy effects and calculate their effect on the hysteresis loop. We consider the wire as a thin chain of polycrystallites whose grain boundaries are at random positions, the average segment length (grain length) being L_g.

When the crystallite size R_0 is smaller than the wall-width parameter $\delta_0 = \sqrt{A/K_u}$ (table 1), then the exchange interaction ensures a cooperative coupling of neighbouring grains, and the localization radius R is governed by the well known three-dimensional scaling result [65]

$$L \sim \frac{\delta_0^3}{L_g}. \tag{26}$$

Essentially, the size L of the correlated regions is a domain-wall width calculated self-consistently from the region's average anisotropy [62, 65].

The bulk result (26) applies to wires where $d_w > L > L_g$. When the wire diameter is comparable to or smaller than the grain size, then there is a transition to a novel, quasi-one-dimensional regime, where one has to distinguish between the two directions along and perpendicular to the wire axis [47]. Figure 16 shows the corresponding phase diagram, whereas the corresponding scaling relations are derived in [47]. This phase diagram provides a qualitative understanding of localization phenomena whose behaviour is governed by the effect of polycrystallinity. In practice, this is realized in the hard-magnetic limit, $K_u \gg M_s^2$. In soft and semihard materials, magnetostatic surface charges reduce the role of the polycrystalline anisotropy [47, 66].

In the limit of strong surface charges, that is, in the case of soft magnets, such as Ni, it is suitable to start from the aligned state. The easy axis $\boldsymbol{n}$ closest to $\boldsymbol{e}_z$ and the normalized magnetization vectors can be written as [66]:

$$\boldsymbol{n}(\boldsymbol{r}) = \sqrt{1 - a^2(\boldsymbol{r})}\boldsymbol{e}_z + \boldsymbol{a}(\boldsymbol{r}) \tag{27}$$

and

$$\boldsymbol{s}(\boldsymbol{r}) = \sqrt{1 - m^2(\boldsymbol{r})}\boldsymbol{e}_z + \boldsymbol{m}(\boldsymbol{r}) \tag{28}$$

where $\boldsymbol{a}(\boldsymbol{r})$ and $\boldsymbol{m}(\boldsymbol{r})$ are the easy-axis and magnetization components perpendicular to the wire (in the film plane). For not-too-large reverse fields we can restrict ourselves to terms linear in the small quantity $\boldsymbol{m}$. Minimizing the total magnetic energy with respect to $\boldsymbol{m}(\boldsymbol{r})$ then yields, in one dimension, the linearized differential equation

$$-A\frac{\mathrm{d}^2\boldsymbol{m}}{\mathrm{d}z^2} + (K_{eff} + \tfrac{1}{2}M_s H)\boldsymbol{m} = K_{eff}\boldsymbol{a}(z). \tag{29}$$

This equation means that the polycrystalline easy-axis disorder $\boldsymbol{a}(z)$ acts as a random inhomogeneity. After some calculations [66], we obtain the result

$$M(H) = M_s\left(1 - \frac{c_0 K_{eff}^2}{4A^2} \times \frac{2\sqrt{K_{eff}/A}\sqrt{1 + M_s H/2K_{eff}} + 1/L}{(K_{eff}/A)^{3/2}(1 + M_s H/K_{eff})^{3/2}(\sqrt{K_{eff}/A}\sqrt{1 + M_s H/2K_{eff}} + 1/L)^2}\right). \tag{30}$$

In this equation, the parameter $c_0 = \langle a^2 \rangle$ describes the strength of the wire disorder and incorporates both magnetocrystalline and magnetostatic contributions. For the considered case of nearly ideal wires we expect that c_0 is much smaller than 1. Here $\kappa = \kappa_0\sqrt{1 + M_s H/2K_{eff}}$ and $\kappa_0 = \sqrt{K_{eff}/A}$.

Figure 17 compares the prediction equation (30) with the experimental hysteresis loop of Ni nanowires having radii of about 5 nm. The best fit is obtained for $c_0 = 0.16$ and $K_{eff} = 0.035$ MJ m^{-3} (3.5×10^5 erg cm^{-3}). From figure 17 we see that the agreement between theory and experiment is excellent unless we approach H_c. The incorrect description of the coercivity is due to the neglect of higher-order perturbation corrections in (29): that

equation is (i) linear and (ii) ignores the micromagnetic localization of the reversal process [66]. The fitted parameter $K_{eff} = 0.035$ MJ m^{-3} is similar to the maximum shape anisotropy constant of 0.078 MJ m^{-3} (7.8×10^5 erg cm^{-3}).

6. Alloy and multilayer systems

Several methods have been employed to modify the coercivity of magnetic nanowire arrays. Kawai *et al* investigated the influence of additives on the coercivity and squareness ratios of Fe, Co, Ni and their alloys [44, 46]. They found that the coercivity increased linearly with increasing Fe content for Fe–Ni alloys, from 700 Oe for Ni to 2300 Oe for Fe. For an Fe–Co alloy, the coercivity peaked at 3200 Oe at the Fe content of about 20%. Although strong magnetic anisotropy in the direction perpendicular to the substrate was observed, anisotropy in the horizontal direction appeared in Co–Ni (50%) alloy. Daimon *et al* found that the addition of Cu and P to the Fe nanowires decreased the coercivity to less than 1000 Oe and P was a more effective additive in decreasing the coercivity [67]. The drastic decrease in coercivity of Fe–P alumite film was ascribed to the discontinuity of the Fe particles, since P precipitates between the Fe microcrystallites.

As mentioned in section 2, to fabricate the nanowire arrays, an alternating current is employed between the alumite template and a suitable counterelectrode since the non-conducting aluminium oxide barrier layer underneath the pores blocks the dc current. It is difficult to use the conventional dc reduction method to produce multilayers or alloys of two metals with large different reduction potentials, such as Co and Cu or Fe and Pt. For the conventional dc reduction method, the corresponding salt solutions are contained in one chemical cell to produce the desired multilayers or alloys and the thickness or composition can be precisely controlled by applying different reduction potentials. Since ac is imposed in fabricating nanowires in alumina templates, a different deposition method must be used. Recently we have succeeded in fabricating Fe/Pt multilayered nanowire arrays by alternating the alumite template between two chemical cells containing Fe and Pt ions using alternating current at a voltage of 20 V and a frequency of 250 Hz [68]. The thickness of individual layers is around 10 nm. The multilayered Fe/Pt nanowires exhibit an easy magnetization along the wire axis, which is probably due to shape anisotropy. Annealing studies led to either two-phase or soft-phase phenomena. Future work will be aimed at studies as a function of layer thicknesses and at achieving higher coercivity and higher anisotropy.

An alternative approach to fabricate alloyed or multilayered nanowires in porous alumites is to remove the bottom barrier layer to form 'through' pores and then to use the conventional dc electro-deposition method. Up until now, work has only been done in commercially available anodic alumina membranes of thickness of 60 μm and quoted pore diameters of 20, 100 and 200 nm [69]. One disadvantage of the commercial membranes is the random spacing of the pores. Furthermore, the large pore diameter may preclude the fabricated nanowires from displaying nanoscale effects. Schwarzacher's group has studied the Co–Cu alloy nanowires [70] and Co–Ni–Cu/Cu multilayered nanowires [71] electro-deposited into commercial anodic membranes. A gold layer has been evaporated on one side of the membrane to serve as a conducting electrode. The thickness or composition was controlled by the applied reduction potential. They found a large value of the current perpendicular to plane giant magnetoresistance (CPP-GMR) for Co–Ni–Cu (5.4 nm)/Cu (2.1 nm) multilayered nanowires: 55% at room temperature and 115% at 77 K.

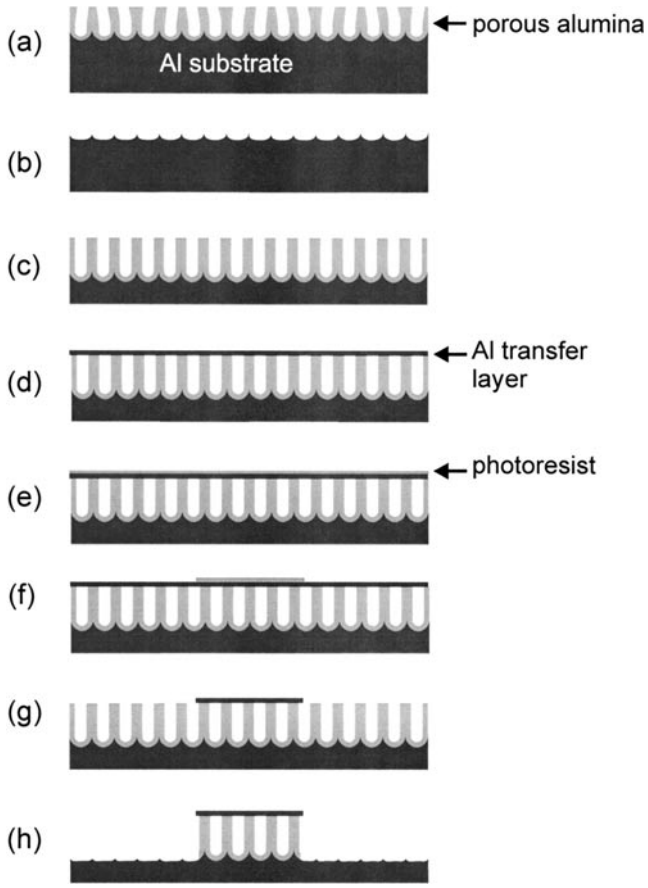

Figure 18. Schematic diagram of the fabrication and microstructuring of a nanopore array in anodic alumina: (a) porous alumina obtained in the first anodization, (b) remaining pits on the aluminium surface after removal of the porous alumina, (c) nanopore arrays formed after the second anodization, (d) evaporating an aluminium transfer layer, (e) coating of photoresist, (f) patterning of resist, (g) patterning of aluminium by a wet chemical etch based on phosphoric and nitric acid with an additional small amount of wetting agent (the Al layer not covered by the resist was completely removed after 30 min of etching), (h) etching of vertical microstructures by etching in an aqueous H_3PO_4 solution (5 wt%). Since in the opened area the solution can penetrate into the holes, the etching takes place at the whole oxide/solution interface. The Al-mask-covered part is not attacked by the etching solution, resulting in the desired pattern. (Courtesy A-P Li.)

7. Outlook and conclusions

Possible applications for the self-assembled magnetic nanowire arrays are patterned magnetic media, magnetic devices and materials for microwave applications. Self-assembled alumites can also serve as evaporation/sputtering masks to produce patterned dot arrays as suggested by Masuda and Satoh [20]. The regimented ordering can be achieved by a moulding process [72]. An appropriate master was introduced to texture the Al surface to guide the growth of channels and to offer high-throughput mass production, which can overcome the bottleneck in the conventional nanolithographic process. Li *et al* used a microstructuring process to make bars of porous alumina for applications as photonic crystals [73]. Figure 18 shows a schematic diagram of the process. The resulting bars were 100–400 μm wide, 100–300 μm

high and several millimetres long. A similar technique can be applied to manufacture magnetic devices.

We have seen in this review that a great deal has been learned about synthetic processes and control of the dimensions and magnetic properties of nanoscale magnetic wires electrodeposited in self-assembled pores. Much progress has been made in understanding the magnetic properties of these systems. In particular, we now understand the crucial effect of wire imperfections, which give rise to deviations from coherent-rotation or curling behaviour and determine the coercivity and magnetic viscosity of the wire arrays. The corresponding magnetic localization has been analysed for a variety of model systems, but full-scale simulations of real structures remain a challenge to future research. Compared to the behaviour of individual wires, interactions between wires are of secondary importance and can be approximated by a demagnetizing field. There is great potential in the near future for further development of exquisite forms of these nanoscale systems including hybrid ones involving magnetic and semiconducting or other functional components. Development of magnetic or electronic device applications based on these nanostructures is now on the horizon. With sufficient allocation of resources from various nanotechnology initiatives, the future of science and application of these systems looks very bright.

Acknowledgments

This work has been supported by NSF, NRI and CMRA. We are indebted for assistance and helpful discussions to S Bandyopadhyay, A-P Li, Y Liu, S-H Liou, H Zeng and L Menon.

References

[1] Chou S Y, Wei M, Krauss P R and Fisher P B 1994 *J. Vac. Sci. Technol.* B **12** 3695
[2] Hehn M, Ounadjela K, Bucher J, Rousseaux F, Decanini D, Bartenlian B and Chappert C 1995 *Science* **272** 1782
[3] Roxlo B, Deckman H W, Gland J, Cameron S D and Cianelli R 1987 *Science* **235** 1629
[4] Masuda H and Fukuda K 1995 *Science* **268** 1466
[5] Sugawara A, Streblechenko D, McCartney M and Scheinfein M R 1998 *IEEE Trans. Magn.* **34** 1081
[6] Ozin G A 1992 *Adv. Mat.* **4** 612
[7] Martin C R 1994 *Science* **266** 1961
[8] Fert A and Piraux L 1999 *J. Magn. Magn. Mater.* **200** 338 and references therein
[9] Routkevitch D, Tager A A, Haruyama J, AlMawlawi D, Moskovits M and Xu J M 1996 *IEEE Trans. Magn.* **43** 1646
[10] Keller F, Hunter M S and Robinson D L 1953 *J. Electrochem. Soc.* **100** 411
[11] Kawai S and Ueda R 1975 *J. Electrochem. Soc.* **122** 32
[12] Shiraki M, Wakui Y, Tokushima T and Tsuya N 1985 *IEEE Trans. Magn.* **21** 1465
[13] Saito M, Kirihara M, Taniguchi T and Miyagi M 1989 *Appl. Phys. Lett.* **55** 607
[14] Mizuki I, Yamamoto Y, Yoshino T and Baba N 1987 *J. Met. Surf. Finish. Soc. Japan* **38** 561
[15] Li F-Y, Zhang L and Metzger R M 1998 *Chem. Mater.* **10** 2470
Li F Y and Metzger R M 1997 *J. Appl. Phys.* **81** 3806
[16] Liu Y 2000 private communication
[17] Li A P, Müller F, Birner A, Nielsch K and Gösele U 1998 *J. Appl. Phys.* **84** 6023
[18] O'Sullivan J P O and Wood G C 1970 *Proc. R. Soc.* A **317** 511
[19] Jessensky O, Müller F and Gösele U 1998 *J. Electrochem. Soc.* **145** 3735
[20] Masuda H and Satoh M 1996 *Japan. J. Appl. Phys.* II **35** L126
[21] Van der Linden B, Terryn H and Vereechen J 1990 *J. Appl. Electrochem.* **20** 798
[22] Moskovits M *et al* 1993 *US Patent 5202290*
AlMawlawi D, Coombs N and Moskovits M 1991 *J. Appl. Phys.* **70** 4421
[23] Menon L, Zheng M, Zeng H, Bandyopadhyay S and Sellmyer D J 2000 *J. Electron. Mater.* **29** 510
[24] Zeng H, Zheng M, Liu Y, Menon L, Bandyopadhyay S and Sellmyer D J 2000 unpublished

[25] Metzger R M, Konovalov V V, Sun M, Xu T, Zangari G, Xu B, Benakli M and Doyle W D 2000 *IEEE Trans. Magn.* **36** 30
[26] AlMawlawi D, Liu C Z and Moskovits M 1994 *J. Mater. Res.* **9** 1014
[27] Skomski R and Coey J M D 1999 *Permanent Magnetism* (Bristol: Institute of Physics)
[28] Stoner E C and Wohlfarth E P1948 *Phil. Trans. R. Soc.* A **240** 599
[29] Henkel D 1964 *Phys. Status Solidi* **7** 919
[30] Wohlfarth E P 1958 *J. Appl. Phys.* **29** 595
[31] Skomski R, Liu J-P and Sellmyer D J 1999 *Phys. Rev.* B **60** 7359
[32] Kronmüller H, Durst K D and Sagawa M 1988 *J. Magn. Magn. Mater.* **74** 291
[33] Becker R and Döring W 1939 *Ferromagnetismus* (Berlin: Springer)
[34] Néel L 1949 *Ann. Geophys.* **5** 99
[35] Street R and Wooley J C 1949 *Proc. Phys. Soc.* A **62** 562
[36] Gaunt P 1986 *J. Appl. Phys.* **59** 4129
[37] E. Kneller E 1966 Theorie der Magnetisierungskurve kleiner Kristalle *Handbuch der Physik XIII/2: Ferromagnetismus* ed H P J Wijn (Berlin: Springer) p 438
[38] Sellmyer D J, Yu M, Thomas R A, Liu Y and Kirby R D 1998 *Phys. Low-Dim. Struct.* **1/2** 155
[39] Sellmyer D J, Yu M and Kirby R D 1999 *Nanostruct. Mater.* **12** 1021
[40] Givord D, Lu Q, Rossignol M F, Tenaud P and Viadieu T 1990 *J. Magn. Magn. Mater.* **83** 183
[41] Givord D, Lienard A, Tenaud P and Viadieu T 1987 *J. Magn. Magn. Mater.* **67** L281
[42] Huysmans G T A and Lodder J C 1988 *J. Appl. Phys.* **64** 2016
[43] Zeng H, Zheng M, Skomski R, Sellmyer D J, Liu Y, Menon L and Bandyopadhyay S 2000 *J. Appl. Phys.* **87** 4718
[44] Kawai S and Ueda R 1975 *J. Electrochem. Soc.* **122** 32
[45] Zangari G and Lambeth D N 1997 *IEEE Trans. Magn.* **33** 3010
[46] Kawai S and Ishiguro I 1976 *J. Electrochem. Soc.* **123** 1047
[47] Skomski R, Zeng H, Zheng M and Sellmyer D J 2000 *Phys. Rev.* B **62** 3900
[48] Zheng M, Menon L, Zeng H, Liu Y, Bandyopadhyay S, Kirby R D and Sellmyer D J 2000 *Phys. Rev.* B **62** 12 282
[49] Yang S G, Zhu H, Ni G, Yu D L, Tang S L and Du Y W 2000 *J. Phys. D: Appl. Phys.* **33** 2388
[50] Li F 1995 *PhD Thesis* University of Alabama
[51] Wirth S, Field M, Awschalom D D and von Molnár S 1998 *Phys. Rev.* B **57** R14 028
[52] Grobert N, Hsu W K, Zhu Y Q, Hare J P, Kroto H W and Walton D R M 1999 *Appl. Phys. Lett.* **75** 3363
[53] Aharoni A 1996 *Introduction to the Theory of Ferromagnetism* (Oxford: Oxford University Press)
[54] Skomski R and Sellmyer D J 2001 *J. Appl. Phys.* at press
[55] O'Barr R and Schultz S 1997 *J. Appl. Phys.* **81** 5448
Lederman M, O'Barr R and Schultz S 1995 *IEEE Trans. Magn.* **31** 3793
Lederman M, O'Barr R and Schultz S 1993 *J. Appl. Phys.* **73** 6961
[56] Wernsdorfer W, Doudin B, Mailly D, Hasselbach K, Benoit A, Meier J, Ansermet J-Ph and Barbara B 1996 *Phys. Rev. Lett.* **77** 1873
Wegrowe J E, Kelly D, Fromck A, Gilbert S E and Ansermet J-Ph 1999 *Phys. Rev. Lett.* **82** 3681
[57] Skomski R 1998 *J. Appl. Phys.* **83** 6503
[58] Anderson P W 1958 *Phys. Rev.* **109** 1492
[59] Imry Y and Ma Sh-K 1975 *Phys. Rev. Lett.* **35** 1399
[60] Sellmyer D J and Nafis S 1986 *Phys. Rev. Lett.* **57** 1173
[61] Alben R, Becker J J and Chi M C 1978 *J. Appl. Phys.* **49** 1653
[62] Chudnovsky E M, Saslow W M and Serota R A 1986 *Phys. Rev.* B **33** 251
[63] Skomski R 1996 *J. Magn. Magn. Mater.* **157–158** 173
[64] Richter J and Skomski R 1989 *Phys. Status Solidi* b **153** 711
[65] Alben R, Chi M C and Becker J J 1978 *J. Appl. Phys.* **49** 1653
[66] Zheng M, Skomski R, Liu Y and Sellmyer D J 2000 *J. Phys.: Condens. Matter* **12** L497
[67] Daimon H, Kitakami O, Inagoya O and Sakemoto A 1991 *Japan. J. Appl. Phys.* **30** 282
[68] Zheng M, Liu Y, Zeng H, Bandyopadhyay S, Kirby R D and Sellmyer D J 2000 *APS March Meeting*
[69] Rigby W R, Cowieson D R, Davies N C and Furneaux R C 1990 *Trans. Inst. Metal Finish* **68** 95
[70] Blythe H J, Fedosyuk V M, Kasyutich O I and Schwarzacher W 2000 *J. Magn. Magn. Mater.* **208** 251
[71] Evans P R, Yi G and Schwarzacher W 2000 *Appl. Phys. Lett.* **76** 481
[72] Masuda H, Yamada H, Satoh M, Asoh H, Nakao M and Tamamura T 1997 *Appl. Phys. Lett.* **71** 2770
[73] Li A-P, Müller F, Birner A, Nielsch K and Gösele U 1999 *Adv. Mater.* **11** 483
[74] Skomski R, Kirby R D and Sellmyer D J 1999 *J. Appl. Phys.* **85** 5069